

Title: Observation of room-temperature polar skyrmions

S. Das^{1,17*}, Y. L. Tang^{1,2,17}, Z. Hong^{3,17}, M. A. P. Gonçalves^{4,17}, M. R. McCarter⁵, C. Klewe⁶, K. X. Nguyen⁷, F. Gómez-Ortiz⁸, P. Shafer⁶, E. Arenholz⁶, V. A. Stoica⁹, S.-L. Hsu^{1,10}, B. Wang³, C. Ophus¹⁰, J. F. Liu¹¹, C. T. Nelson¹², S. Saremi¹, B. Prasad¹, A. B. Mei¹³, D. G. Schlom^{13,14}, J. Íñiguez^{4,15}, P. García-Fernández⁸, D. A. Muller^{14,16}, L. Q. Chen³, J. Junquera⁸, L. W. Martin^{1,2}, R. Ramesh^{1,2,5*}

¹*Department of Materials Science and Engineering, University of California, Berkeley, CA, USA.*

²*Materials Sciences Division, Lawrence Berkeley National Laboratory, Berkeley, CA, USA.*

³*Department of Materials Science and Engineering, The Pennsylvania State University,*

University Park, PA, USA. ⁴*Materials Research and Technology Department, Luxembourg*

Institute of Science and Technology (LIST), Esch/Alzette, Luxembourg. ⁵*Department of Physics,*

University of California, Berkeley, CA, USA. ⁶*Advanced Light Source, Lawrence Berkeley*

National Laboratory, Berkeley, CA, USA. ⁷*Department of Chemistry and Chemical Biology,*

Cornell University, Ithaca, NY, USA. ⁸*Departamento de Ciencias de la Tierra y Física de la*

Materia Condensada, Universidad de Cantabria, Santander, Spain. ⁹*Department of Materials*

Science and Engineering, Pennsylvania State University, University Park, PA, USA. ¹⁰*National*

Center for Electron Microscopy, Molecular Foundry, Lawrence Berkeley National Laboratory,

Berkeley, CA, USA. ¹¹*Molecular Foundry, Lawrence Berkeley National Laboratory, Berkeley,*

CA, USA. ¹²*Center for Nanophase Materials Sciences, Oak Ridge National Laboratory, Oak*

Ridge, TN, USA. ¹³*Department of Materials Science and Engineering, Cornell University,*

Ithaca, NY, USA. ¹⁴*Kavli Institute at Cornell for Nanoscale Science, Ithaca, NY, USA.* ¹⁵*Physics*

and Material Science Research Unit, University of Luxembourg, Belvaux, Luxembourg. ¹⁶*School*

of Applied and Engineering Physics, Cornell University, Ithaca, NY, USA. ¹⁷*These authors*

*contributed equally: S. Das, Y. L. Tang, Z. Hong, M. A. P. Gonçalves. *e-mail:*

sujitdas@berkeley.edu; rramesh@berkeley.edu

Complex topological configurations are fertile ground for exploring emergent phenomena and exotic phases in condensed-matter physics. For example, the recent discovery of polarization vortices and their associated complex-phase coexistence and response under applied electric fields in superlattices of $(\text{PbTiO}_3)_n/(\text{SrTiO}_3)_n$ suggests the presence of a complex, multi-dimensional system capable of interesting physical responses, such as chirality, negative capacitance and large piezo-electric responses¹⁻³. Here, by varying epitaxial constraints, we discover room-temperature polar-skyrmion bubbles in a lead titanate layer confined by strontium titanate layers, which are imaged by atomic-resolution scanning transmission electron microscopy. Phase-field modelling and second-principles calculations reveal that the polar-skyrmion bubbles have a skyrmion number of +1, and

resonant soft-X-ray diffraction experiments show circular dichroism, confirming chirality. Such nanometre-scale polar-skyrmion bubbles are the electric analogues of magnetic skyrmions and could contribute to the advancement of ferroelectrics towards functionalities incorporating emergent chirality and electrically controllable negative capacitance.

Topological patterns in magnetic systems (for example, skyrmions) have garnered enormous interest in condensed-matter physics, as well as for potential applications in spintronics or skyrmionics⁴⁻⁷, including the design of racetrack memories^{8,9}. This raises the question of whether analogous arrangements of electrical dipoles (that is, polar skyrmions) can be realized. $(\text{PbTiO}_3)_n/(\text{SrTiO}_3)_m$ heterostructures provide an intriguing opportunity to test for this possibility, since researchers have already demonstrated the formation of emergent polar topologies, such as chiral vortices^{1,3}, ferroelectric chiral and achiral domain walls^{10,11} or ferroelectric bubble domains¹². Theoretical predictions suggest that there is considerable potential for obtaining bubble-shaped nanodomains¹³ and skyrmion-like topological structures in ferroelectric materials driven by the interplay of elastic, electrostatic and gradient energies¹⁴⁻¹⁷. By recognizing the crucial role of lattice-mismatch strain, we demonstrate the formation of chiral, polar-skyrmion bubbles with a skyrmion number of +1 using a combination of real-space imaging, second-principles ab initio calculations and phase-field modelling.

Heterostructures of $[(\text{PbTiO}_3)_n/(\text{SrTiO}_3)_m]_m$ ($n = 12-20$, $m = 1-8$) were fabricated on TiO_2 -terminated single-crystalline SrTiO_3 (001) substrates by reflection high-energy electron diffraction (RHEED)-assisted pulsed-laser deposition (Methods)¹. Three-dimensional reciprocal space mapping (RSM) of the trilayer ($m = 1$) and superlattice ($m = 8$) structures (Extended Data Fig. 1) about the 003 diffraction condition shows satellite peaks about the film peak along the in-plane directions (side lobes, Extended Data Fig. 1a, c), corresponding to an ordered phase with a periodicity of about 8 nm. The intensity distribution shows a ring with a preference for alignment along the cubic directions of the substrate (Extended Data Fig. 1b, d). The appearance of such a textured ring in reciprocal space can arise from ferroelectric nanodomains¹⁸. The RSM indicates consistency between the trilayer and superlattice on SrTiO_3 , where the ring size and its in-plane widths (Extended Data Fig. 1g, h) are nearly the same, but very distinct from periodic vortex nanodomains observed previously² on DyScO_3 (Extended Data Fig. 1e, f). To clarify the source of

this diffraction pattern, we present real-space imaging results obtained by transmission electron microscopy (TEM).

Cross-sectional dark-field TEM for trilayer ($m = 1$) (Fig. 1a) and superlattice ($m = 8$) (Fig. 1b) structures reveals intensity modulations with a length scale of about 8 nm, suggesting the formation of antiparallel polar regions. Examining the corresponding planar-section images, taken using scanning transmission electron microscopy (STEM), trilayers exhibit a mixture of circular (about 8 nm diameter) and elongated features (Fig. 1c), whereas the superlattices predominantly exhibit arrays of circular features (about 8 nm diameter; Fig. 1d, Extended Data Fig. 2). Certainly, the topology of these domain walls is distinct, in that they are broken up into many regions of shorter-range order along multiple in-plane directions, leading to distinct circular and elongated textures (Fig. 1, Extended Data Figs. 2, 3), which were not observed in previously studied vortex arrays¹ (Extended Data Fig. 3). Consistent with the X-ray RSM studies, fast Fourier transforms (FFT) of the images reveal side lobes with a fourfold symmetry (insets, Fig. 1c, d). It is noteworthy that the in-plane modulation of about 8 nm is identical to that observed in RSM studies. Such features closely resemble the results of phase-field simulations (Extended Data Fig. 4a–d), where the blue markers represent in-plane polarization (P_{ip}), whereas the white regions have out-of-plane polarization (P_{op}). Here, we see the formation of these features in plain view, where circular regions of P_{op} are surrounded by P_{ip} borders with Néel-like rotation of the polarization.

Second-principles ab initio calculations¹⁹ were used to examine the microscopic details of these polarization textures. With these calculations, we show that they are analogous to magnetic skyrmions and have a mathematically definable and characteristic skyrmion number (Methods). These calculations show that the local electric dipoles continuously rotate both in- and out-of-plane at the $\text{PbTiO}_3/\text{SrTiO}_3$ boundary (Fig. 2a, b). At the top and bottom of the PbTiO_3 layer, the electric dipoles display an in-plane polarization connecting the up and down polar regions with diverging and converging polarization, respectively (Fig. 2c, e). Superimposed on this hedgehog-like, cylindrically symmetric polar texture, we observe the condensation of a curling polarization pattern in the middle x-y plane of the PbTiO_3 layer (Fig. 2b, d), which is also indicated from phase-field simulations at 0 K and 298 K (Extended Data Fig. 4e-h).

Analysis of the polarization texture at the top and bottom PbTiO₃/SrTiO₃ interfaces (Fig. 2c, e) reveals hedgehog-like (Néel) skyrmion structures, whereas in the middle PbTiO₃ layer (Fig. 2d) a “combed hedgehog” (Bloch) skyrmion is observed. In addition, we identify a polarization texture where the local order parameter has a null rotational component, but a positive divergence (Fig. 2c) at the top plane. The reverse happens at the bottom plane (Fig. 2e), with an inward-pointing local polarization profile (negative divergence). At the middle layer, the in-plane component of the polarization displays only a component parallel to the domain wall, as in conventional Bloch skyrmions (Fig. 2d). From this, we see that the three-dimensional polar-skyrmion bubble can be described as an evolution of two-dimensional skyrmions along the film normal (from top to bottom in a single PbTiO₃ layer, going from a hedgehog to a vortex to a hedgehog structure). This complex polar evolution – including the formation of the in-plane Bloch component – arises from the presence of a strong depolarization field. Despite this evolution, these structures are topologically equivalent because they can be transformed into each other by a continuous deformation²⁰. The class of these topological structures can be indexed by a skyrmion number, defined as¹⁴

$$N_{\text{sk}} = \frac{1}{4\pi} \iint \mathbf{u} \cdot \left(\frac{\partial \mathbf{u}}{\partial x} \times \frac{\partial \mathbf{u}}{\partial y} \right) dx dy \quad (1)$$

where \mathbf{u} denotes the normalized local dipole moment, and the surface integral is taken over the corresponding (001) plane. The integrand of equation (1), the Pontryagin density, is also plotted in Fig. 2f-h. For this system, $N_{\text{sk}} = +1$ is an integer that is invariant for every plane (Methods). It is also interesting and important to note that even the elongated polar regions observed in the TEM images (Fig. 1c, Extended Data Fig. 5) manifest a skyrmion number of +1, indicating that they have the same topology.

To elucidate the atomic structure of the skyrmion bubble, we carried out atomic-scale polarization mapping using a displacement vector-mapping algorithm on both plan view and cross-sectional high-angle annular dark-field (HAADF)-STEM images, along with four-dimensional STEM (4D-STEM) with an electron microscope pixel array detector (EMPAD)²¹ (Fig. 3, Extended Data Fig. 6; details in Methods)²². Titanium-displacement vector mapping analysis of the plane-view HAADF-STEM image (Extended Data Fig. 6a) reveals the microscopic displacement field around a single skyrmion bubble (Extended Data Fig. 6b). The vector map (Fig. 3a) corresponding

to this image of a single skyrmion bubble (white circle, Extended Data Fig. 6a) shows a region where the reversed titanium displacement is converging from the edge to the centre, reminiscent of a hedgehog-like skyrmion structure²³. In cross-sectional HAADF-STEM images (Fig. 3c), vector displacement mapping clearly shows a cylindrical polar region with anti-parallel (up-down) polarization. The polarization vector rotates at the boundaries near the $\text{PbTiO}_3/\text{SrTiO}_3$ interfaces, consistent with the divergence of polarization observed in the plane-view images. The combined plane-view and cross-sectional vector displacement mapping reveals a hedgehog-like structure at the top of the PbTiO_3 layer, consistent with the second-principles calculations (Fig. 2).

In 4D-STEM, the full momentum distribution is collected at every scan position, and in polar materials the asymmetry in scattering intensity between conjugate diffracted beams reflects the crystal polarity (Extended Data Fig. 7; details in Methods)²⁴. The first moments of the beams give a probability current-flow vector map that is proportional to the in-plane polar order at each beam position. The constant of proportionality is depth-dependent as a result of electron channeling changing the shape of the beam. As an example, the annular dark-field (ADF) image (Fig. 3d) and the in-plane probability current flow (\mathbf{p}) of a skyrmion bubble (Fig. 3e) from a $[(\text{PbTiO}_3)_{16}/(\text{SrTiO}_3)_{16}]_8$ superlattice are shown. To understand the depth dependence of the plane-view images, multiple-scattering calculations of electron beam propagation through the model skyrmion bubble (Fig. 2) were performed using the multislice method²⁵ to produce the simulated ADF (Fig. 3f) and \mathbf{p} (Fig. 3g) maps. These simulations show that the electron scattering signal in 4D-STEM is largely weighted towards the Bloch-like component in the middle of the skyrmion bubble, rather than being a simple uniformly depth-weighted projection. The scalar ADF signal is sensitive to in-plane displacements of the atom columns leading to a strong dechannelling signal from the waist of the skyrmion bubble structure. The probability current flow captures the polar order from the middle and some of the upper portion of the skyrmion bubble, showing a Bloch-like character in both simulation and experiment.

These data, collectively, point to the formation of a polar-skyrmion structure with hedgehog-like components, where the polarization direction rotates smoothly from up to down and from the center to the edge of the skyrmion; along with a Bloch-like, in-plane component, consistent with the theoretical predictions. The diverging and converging polarization rotation at the top and bottom of the polar structure resembles the spin configuration of Néel skyrmions in

ferromagnets²⁶. Associated with the realization of such a polar-skyrmion bubble, we anticipated the emergence of interesting properties, such as chirality and a non-zero skyrmion number.

To probe this potential chirality, resonant soft-X-ray diffraction (RSXD) studies were performed on a $[(\text{PbTiO}_3)_{16}/(\text{SrTiO}_3)_{16}]_8$ superlattice (Fig. 4, Extended Data Figs. 8, 9; Methods). According to the calculated structure (Fig. 2), an imaginary line along any direction within the central plane of each PbTiO_3 layer crosses only Bloch domain walls, so that along that line the local polarization exhibits a helical rotation. This helical polarization texture (embedded within the surrounding skyrmions) is virtually identical to the helical polarization configuration that emerges in polar-vortex arrays³ (Extended Data Fig. 8) and should therefore result in a similar dichroic signal from the chiral electronic structure.

A hard-X-ray RSM study about the 002-diffraction condition (Fig. 4a) shows the presence of two sets of ordering. First, there are regular peaks along the out-of-plane direction, related to the out-of-plane periodicity of the superlattice (about 12 nm). Second, there are satellite peaks in the perpendicular or in-plane direction, corresponding to the in-plane ordering of the polar structures (about 8 nm). RSXD studies were performed at satellite peaks near the reciprocal lattice vector components $(Q_x, Q_y, Q_z) = (0, 0, \ll 2\pi/c)$ (one such peak is shown in Fig. 4b; Methods). Because the X-ray energy is tuned through the titanium L_3 and L_2 absorption edges, the intensity of the satellite diffraction peaks is sensitive to periodic distortions, specifically chiral arrangements of the anisotropic titanium orbitals. By measuring the spectra with both right and left-circularly polarized light (Fig. 4c), subtracting the background fluorescence (Fig. 4d), and taking the difference between the two spectra (Fig. 4e), the X-ray circular dichroism (XCD) can be measured. The clear dichroism at the L_3 edge corresponding to the t_{2g} states³ is indicative of chiral structures. We note that circular dichroism is observed for both the superlattice and trilayer structures (Fig. 4, Extended Data Fig. 9). Theoretical reports have shown that a likely explanation for the nonmagnetic circular dichroism is a chiral configuration of charge quadrupole moments²⁷. This chiral configuration is composed of a helical rotation of titanium t_{2g} orbitals, which possess a quadrupole moment and are related to the ferroelectric distortions of TiO_6 octahedra. The XCD observed here is consistent with the presence of Bloch domain walls in the PbTiO_3 layers.

Additionally, resonant scattering intensity and circular dichroism were measured as a function of the lateral scattering vector (Fig. 4f, Extended Data Fig. 10a). The polarization-averaged scattering intensity exhibits a clear asymmetry under reversal of the scattering vector (Extended Data Fig. 10b). The presence of the Bloch component will lead to a breaking of Friedel's law in resonant diffraction experiments because of the broken inversion symmetry along the in-plane directions. Therefore, the observed asymmetry in the intensity of mirrored diffraction peaks provides strong evidence for the Bloch component of polarization in the skyrmion bubbles. Furthermore, as the lateral scattering vector Q_y is reversed, the sign of the XCD also reverses, which is a telltale signature of chirality^{3,27}. The simplest explanation for both the asymmetric diffraction intensity and the measured circular dichroism is a Bloch component of polarization, because it is the simplest structure to exhibit broken inversion symmetry as well as chirality. This, along with the atomic-scale images and computational studies, confirms the presence of a polar-skyrmion bubble structure.

In summary, we report the observation of polar-skyrmion bubbles in a confined PbTiO_3 layer. This is the first observation of this intriguing electric skyrmion structure, which is composed of a superposition of Néel and Bloch textures, in any ferroic material. This structure resembles vortex rings previously described in the context of topological semimetals²⁸, superfluids²⁹ and quantum chromodynamics³⁰, and three-dimensional skyrmions and solitons that have been predicted and observed in ultra-cold gases (that is, Bose-Einstein condensates)^{31,32}. Such a three-dimensional structure deviates from the ordinary two-dimensional skyrmions observed in magnetic systems. Although three-dimensional, tube-like skyrmions or three-dimensional skyrmion lattices exist³³, they are different from this new polar-skyrmion bubble phase. The stabilization of such non-uniform polarization topology results in highly enhanced susceptibilities and provides a pathway for engineering functionalities previously inaccessible in these materials. Furthermore, if ferroelectric skyrmions can be moved with an electric field, they could be employed to create novel device architectures.

METHODS

Sample preparation using RHEED-assisted pulsed-laser deposition. n - SrTiO_3/n - PbTiO_3/n - SrTiO_3 trilayers (n is the number of monolayers) and $[(\text{PbTiO}_3)_n/(\text{SrTiO}_3)_n]_m$ superlattices were

synthesized on TiO₂-terminated single-crystalline SrTiO₃ (001) substrates via RHEED-assisted pulsed-laser deposition (KrF laser). The growth temperature and oxygen pressure for the bottom SrTiO₃ layer were 700 °C and 50 mtorr, respectively. The PbTiO₃ and the top SrTiO₃ layer were grown at 610 °C in 100 mtorr oxygen pressure. For all materials, the laser fluence was 1.5 J cm⁻² with a repetition rate of 10 Hz. RHEED was used during the deposition to ensure the maintenance of a layer-by-layer growth model for both PbTiO₃ and SrTiO₃. The specular RHEED spot was used to monitor the RHEED oscillations. After deposition, the heterostructures were annealed for 10 min in oxygen pressure of 50 torr to promote full oxidation and then cooled to room temperature at the same oxygen pressure.

Structural analysis. *Laboratory-based X-ray diffraction.* Structural characterization of the heterostructures was carried out using a Panalytical X'Pert Pro X-ray Diffraction (XRD) system with Cu-K_α radiation (wavelength $\lambda = 1.5405 \text{ \AA}$). The high crystalline quality of the films and the smooth nature of the interfaces were confirmed from X-ray reflectivity and θ - 2θ symmetric XRD scans around the 002 reflection plane, which showed strong superlattice peaks and Laue oscillations (not shown).

Synchrotron XRD. To obtain a comprehensive picture of the crystal structure of the trilayers and superlattices, as well as information on the in-plane and out-of-plane ordering, further structural characterization was done using synchrotron-based XRD. The synchrotron XRD studies were performed at the Sector 33-BM-C and Sector 7-ID-C beamline of the Advanced Photon Source at Argonne National Laboratory, USA. The high flux from the synchrotron X-ray source delivered at this beamline permits the detection of the weak diffracted intensities arising from the lattice modulations associated with the polar-skyrmion bubbles present in the trilayers and superlattices (Extended Data Fig. 1). A double crystal monochromator, in conjunction with two mirrors, was used to deliver a highly monochromatic beam with negligible contamination from higher harmonics. Moreover, the excellent angular accuracy of the Huber 4-circle diffractometer at Sector 33-BM-C and the Newport 6-circle diffractometer (20 keV) at Sector 7-ID-C allowed us to determine the orientation of our crystals very reliably and to obtain three-dimensional (3D) RSMs with high accuracy. Lastly, the availability of the PILATUS 100K pixel detector was essential for the efficient acquisition of 3D RSMs.

STEM. The plane-view samples of the SrTiO₃/PbTiO₃/SrTiO₃ trilayers and superlattices for the STEM experiments were prepared by gluing a 2.5 mm × 2.5 mm film on a 3-mm molybdenum grid. The plane-view samples were then grinded, dimpled and ion-milled. Cross-sectional samples for the dark-field TEM and STEM experiments were prepared by slicing, gluing, grinding, dimpling and ion milling. A Gatan PIPS II was used for the final ion milling. Before ion milling, the samples were dimpled down to less than 20 μm. The final ion-milling voltage was 0.5 kV to reduce ion-beam damage. HAADF-STEM images were recorded by using a Cs-corrected TEAM1 FEI Titan microscope working at 300 kV. A HAADF detector acquiring “Z-contrast” images was used to record the HAADF-STEM images. The beam convergence angle was 17 mrad. The diffraction contrast image (Fig. 1a) was recorded using a TitanX microscope (FEI) working at 300 kV.

Determination and mapping of the polar atomic displacements was performed on the atomic-scale HAADF-STEM images by using the column offsets of each titanium and lead atom, obtained from the position fitting of the titanium and lead atoms¹. The atom positions were determined by fitting them as two-dimensional Gaussian peaks using Matlab. The titanium displacement in each PbTiO₃ unit cell was calculated as a vector between each titanium atom and the center of mass of its four nearest lead neighbors. The displacement of the titanium in each unit cell was opposite to the polarization direction of the PbTiO₃. The visualization of the two-dimensional polar displacement vectors was carried out using Matlab. Random noise in the displacement vector maps was reduced using a weighted smoothing length of 1.2 nm.

4D-STEM. We performed 4D-STEM using an EMPAD²¹. The full momentum distribution – that is, the electron diffraction pattern – was collected at every scan position by the EMPAD. In our experiments, we used a beam energy of 300 kV and a semi-convergence angle of 1.9 mrad to ensure that the diffracted beams did not overlap, corresponding to a 6.3-Å-wide beam on an aberration-corrected Thermo Fisher Themis-Titan STEM system in nanobeam diffraction mode. From the diffraction patterns collected on the EMPAD, we reconstructed the low-angle ADF image and the probability current flow ($\langle p \rangle$) in x and y giving the vector components of polar order³⁴. We compared our experimental results to multislice simulations of the electron beam propagation through the crystal. For the low-order diffraction beams used to reconstruct $\langle p \rangle$, the simulations show that the largest signal comes from the middle of the skyrmion and is not a simple

projection throughout the beam path. This holds for both the low-angle ADF and $\langle p \rangle$ signals. The higher-angle signals show stronger de-channeling (they are generated by electrons scattered closer to the nucleus, where the scattering probability is much higher). Extended Data Fig. 7 shows the HAADF signal for a 17.2-mrad convergence-angle probe used for atomic-resolution imaging, which shows its highest scattering rate midway through the SrTiO₃ layer and is largely depleted before the PbTiO₃ is reached. By contrast, when the probe is narrowed to 1.7 mrad, close to the EMPAD experimental conditions, the probe is still well focused on the atom columns as it leaves the SrTiO₃ layer and produces a larger signal from the PbTiO₃.

Phase-field modelling. Phase-field simulations were performed to simulate the polar structure of PbTiO₃/SrTiO₃ heterostructures on a STO substrate. The spontaneous polarization vectors (\mathbf{P}_i , $i = \{1, 3\}$) were selected as the order parameters, governed by the time-dependent Ginzburg-Landau equations³⁵:

$$\frac{\partial \mathbf{P}_i}{\partial t} = -L \frac{\delta F}{\delta \mathbf{P}_i} \quad (1)$$

where L and t are the kinetic coefficient and the time, respectively. The total free energy F can be expressed as the volume integration of the individual energy densities, namely, the Landau chemical, mechanical, electrostatic and polar gradient energy densities:

$$F = \int (f_{\text{Landau}} + f_{\text{elastic}} + f_{\text{electric}} + f_{\text{gradient}}) dV \quad (2)$$

Detailed expressions of the energy densities, the numerical treatments, the phase-field equations and the parameters can be found in previous reports³⁶⁻⁴⁰. A three-dimensional mesh of $200 \times 200 \times 350$ was used, with a grid spacing of 0.4 nm. Periodic boundary conditions were assumed in the two in-plane dimensions, whereas a superposition scheme⁴¹ was applied in the thickness dimension. From the bottom to the top, the thickness of the substrate, thin film and air was set to be 30, 280 and 32 grids, respectively, whereas 16 unit cells of PbTiO₃ and 16 unit cells of SrTiO₃ layers were periodically stacked to form the superlattice thin film. A short-circuit electric boundary condition³⁶ was used, where the electric potential at the top of the film and at the film/substrate interface was zero. The mechanical-boundary condition was set such that the stress on the film top was zero, whereas the displacement was set to be zero at the bottom of the substrate, sufficiently far from the substrate/film interface³⁵. A wide range of strain conditions were

simulated with the substrate lattice constant ranging from 3.875 Å to 3.99 Å, with an interval of 0.01 Å. Random noise with a magnitude of 0.0001 C m⁻² was used as the initial condition for the evolution of polarization to simulate the thermal fluctuation during the annealing process.

Second-principles calculations. For computational feasibility, we focused on a representative [(SrTiO₃)₄/(PbTiO₃)₁₀] superlattice periodically repeated in space (20 × 20 × 14 elemental perovskite cells in a periodically repeated simulation box), except in those simulations used to compare with the 4D-STEM experiments, where a (SrTiO₃)₁₆/(PbTiO₃)₁₆ superlattice was used. The search for a stable skyrmion structure was carried out in a two-step process. First, starting from a monodomain, downward-pointing ferroelectric configuration in the PbTiO₃ layer, a cylindrical domain with the opposite polarization was defined. This polydomain structure was used as the initial seed for the structural relaxation at zero temperature.

The second-principles simulations were performed using the same methodology presented in previous works^{42,43}, as implemented in the scale-up package^{19,42}. The interactions inside the PbTiO₃ or SrTiO₃ were described using the potentials for the bulk materials⁴². These potentials give qualitatively correct descriptions for the lattice dynamical properties and structural phase transitions of both materials. Then, we treated the interactions in the interface between PbTiO₃ and SrTiO₃, assuming a simple numerical average for the interactions of the ions pairs touching or crossing the interface. The main effect of the stacking is electrostatic, where long-range dipole–dipole interactions are governed by a bare electronic dielectric constant ϵ_∞ , which is taken as a weighted average of the first-principles results for bulk PbTiO₃ ($8.5\epsilon_0$, where ϵ_0 is the vacuum permittivity) and SrTiO₃ ($6.2\epsilon_0$), with weights reflecting the composition of the superlattice. To preserve the electrostatic energy within each material as close as possible to that of the bulk parent compound, the Born effective charge tensors of the inner atoms were rescaled by $\sqrt{\epsilon_\infty/\epsilon_\infty^{\text{ABO}_3}}$ (where “ABO₃” stands for PbTiO₃ or SrTiO₃, depending on the layer). The second-principles parameters of both materials were fitted from density functional theory imposing a hydrostatic pressure of −11.2 GPa to counter underestimation of the local density approximation of the cubic-lattice constant that was taken as the reference structure. We impose an epitaxial constrain assuming in-plane lattice constants of $a = b = 3.901$ Å forming an angle of $\gamma = 90^\circ$, which correspond to a SrTiO₃ (001)-oriented substrate.

Following this strategy, we are able to construct models for superlattices with arbitrary n -stacking. For the simulations, we used periodically repeated supercells that contained 20×20 elemental perovskite units in plane and one full superlattice period in the out-of-plane direction. To solve the models, we used standard Carlo and Langevin molecular-dynamics methods. At low temperature, only random configurations along the Markov chains that produced a decrease in energy were accepted, following this procedure as an equivalent to structural relaxations to find the ground state.

Finally, the local polarizations were obtained within a linear approximation by computing the product of the atomic displacements measured from the ideal cubic structure with the Born effective charge tensor divided by the volume of the unit cell. The skyrmion number, N_{sk} , was obtained from the local dipoles by computing the normalized polarization field defined along each slice of $20 \times 20 \times 1$ elemental perovskite units in the plane of our supercell, and solving equation (1) by applying the strategy presented in ref. ⁴⁴, obtaining a skyrmion number that corresponds to an integer number.

RSXD. RSXD experiments were performed at the scattering endstation of beamline 4.0.2 at the Advanced Light Source, Lawrence Berkeley National Laboratory. The elliptically polarizing undulator at beamline 4.0.2 allows both the energy and polarization of X-rays to be tuned. The spot size of the X-ray beam used was about $100 \mu\text{m}$ in diameter. Experiments were performed on a $[(\text{PbTiO}_3)_{16}/(\text{SrTiO}_3)_{16}]_8$ superlattice sample as well as a trilayer $(\text{SrTiO}_3)_{16}/(\text{PbTiO}_3)_{16}/(\text{SrTiO}_3)_{16}$ sample. This technique has been used previously to demonstrate the chiral nature of both magnetic and non-magnetic structures, including magnetic domain walls⁴⁵ and polar vortices³, by using the dichroism effects that arise from the magnetic exchange scattering and anisotropic tensor susceptibility scattering, respectively. All data were collected in vacuum, using a $1,024 \times 1,024$ -pixel CCD. The out-of-plane ordering of the superlattice gives rise to specular ‘superlattice peaks’, that is, modulations in the intensity of the specular reflection versus the out-of-plane scattering vector that correspond to the period of the superlattice. In proximity to the third-order superlattice reflection, the lateral satellite intensity from the in-plane skyrmion bubble modulation (for example, Fig. 4b) was measured. At the determined Bragg condition, spectra were collected using both right- and left-circularly polarized X-rays tuned through the Ti L_3 and L_2 absorption edges (445–476 eV), where the diffractometer and sample positions were

adjusted to account for the changes in Bragg angle with energy. Additionally, ‘dark images’ were recorded with no X-rays present. All data were normalized to the incoming beam intensity, and the dark images were subtracted from the diffraction data to remove background from detector dark current. The spectra were then normalized to the pre-edge region near 450-455 eV. Subtraction of the normalized detector images (righthanded minus left-handed) shows that the dichroism is localized at the diffraction peak. An example is shown (Extended Data Fig. 9d, Extended Data Fig. 10c) at the $L_3 t_{2g}$ resonance (457.2 eV) for the trilayer and superlattice, respectively. Spectra were then extracted from several locations on the CCD (Extended Data Fig. 9d), one at the diffraction peak (Fig. 4c, Extended Data Fig. 9a) and two nearby in background regions. To correct for nonlinear background intensity, the average of the background regions was weighted slightly with a 44:56 ratio. This weighted average was subtracted from the spectra at the satellite peak. The resulting spectra (Fig. 4d, Extended Data Fig. 9b) show the resonant diffraction intensity for right- and left-circularly polarized light. The $L_3 t_{2g}$ peak intensity was normalized to 1 in the average spectra (that is, the average of the right- and left-circularly polarized spectra), and the right- and left-circularly polarized spectra were adjusted by the same normalization factor (Fig. 4d, Extended Data Fig. 9b). Then, the difference spectrum was calculated as right- minus left-circularly polarized datasets (Fig. 4e, Extended Data Fig. 9c). The resulting spectra give the XCD. For the superlattice and trilayer samples, the XCD at resonance is found to be $\pm 63\%$ and $\pm 61\%$ of the polarization-averaged t_{2g} peak height. The skyrmion bubble diffraction peaks for both trilayer and superlattice samples exhibit strong XCD, indicative of the chiral nature of the phase. Q -dependent scans were taken at a constant energy near resonance (457.4 eV) while varying the lateral scattering vector Q_y . All data were normalized to the incoming beam intensity, and dark images were subtracted from the diffraction data to remove background from detector dark current. The diffraction intensity for right- and left-circularly polarized light and the polarization-averaged intensity were measured (Extended Data Fig. 10a, b). The XCD was calculated at the satellite peak position as the difference in intensity between right- and left-circularly polarized light.

In addition to their observation in the spectra for right- and left-circularly polarized light, these differences can also be visualized using images from the CCD. For a superlattice sample at energies near the $L_3 t_{2g}$ peak, detector images (Extended Data Fig. 10c) show that the diffraction intensity is considerably enhanced for right-circularly polarized light but barely visible for left-circularly polarized light. The intensity difference between CCD images for right- and left-

circularly polarized light shows that the XCD is localized at the diffraction peak on the detector, indicating that the dichroism is coming from the periodic chiral structures in the superlattice.

The qualitative terminology of skyrmions. There is a general consensus on the phenomenological difference between the topological structure of skyrmions and bubbles^{46,47}. We have compared this with magnetic skyrmions and (chiral) bubbles. The key point to “distinguish magnetic skyrmions from general concepts of bubblelike spin textures” is the fact that “the key antisymmetric chiral Dzyaloshinskii-Moriya interaction (DMI) that stabilizes magnetic skyrmions in chiral magnets gives rise to a uniform spin topology of the involved spin textures over the entire system.”^{26,46,47} On the other hand, in magnetic bubble-like spin textures “the spin chiralities of neighboring magnetic bubbles are random.” In other words, magnetic skyrmions necessarily display a topological charge and arise from the DMI, which gives rise to large regions with well-defined chirality. On the other hand, bubbles appear from magnetic dipolar interactions and may (chiral bubbles) or may not (bubbles) individually display a topological charge/chirality. Even if they display chirality, however, they do not lead to large regions with a preferred handedness.

The objects observed in this work arise from interactions that are quite different from their magnetic equivalents and classifying them according to the predominance of DMI or magnetic dipolar interactions does not seem reasonable. It should be noted, however, that the fundamental outcome of the DMI – namely, breaking inversion symmetry – happens naturally in ferroelectrics. Conversely, as shown in the main text and Figs. 2, 3, our polar structures display a well-defined topological charge and chirality individually. Such a chirality is manifested in a macroscopic measurement through XCD observed in resonant X-ray scattering studies (Fig. 4), and the chirality is macroscopically maintained over large length scales (millimeters), which has been observed in spatially resolved resonant scattering studies. This macroscopic ordering of the polar texture is closely related with the notion of magnetic skyrmions in the literature. Thus, we believe that denoting these structures as polar skyrmions is a sensible choice.

Acknowledgements

S.D. acknowledges support from the Gordon and Betty Moore Foundation’s EPiQS Initiative, under grant GBMF5307. Funding for the synthesis and characterization work (to A.B.M., D.G.S. and R.R.) was also provided by the Army Research Office under grant W911NF-16-1-0315.

Y.L.T. and R.R. acknowledge support by the U.S. Department of Energy, Office of Science, Office of Basic Energy Sciences, Materials Sciences and Engineering Division, under contract number DE-AC02-05-CH11231 (Quantum Materials program KC2202) for detailed polarization vector analysis. M.R.M. acknowledges support from the National Science Foundation Graduate Research Fellowship under grant number DGE-1106400. M.A.P.G. and J.Í. are funded by the Luxembourg National Research Fund through the CORE programme (grant FNR/C15/MS/10458889 NEWALLS). Z.H. acknowledges support from the National Science Foundation (DMR-1210588). F.G.-O., P.G.-F. and J.J. acknowledge financial support from the Spanish Ministry of Economy and Competitiveness through grant number FIS2015-64886-C5-2-P, and P.G.-F. acknowledges support from Ramón y Cajal grant number RyC-2013- 12515. L.Q.C. is supported by the US DOE, Office of Basic Energy Sciences under award FG02-07ER46417. V.A.S. acknowledges support from the US DOE, Office of Science, Office of Basic Energy Sciences, under award number DE-SC- 0012375. M.R.M. and S.D. acknowledges use of the Advanced Photon Source, which was supported by the US DOE, Office of Science, Office of Basic Energy Science (DE-AC02-06CH11357), for the synchrotron-based reciprocal space map studies of samples at the Sector 33-BM-C and 7-ID-C beamline. This research used resources of the Advanced Light Source, which is a DOE Office of Science User Facility, under contract number DE-AC02-05CH11231. L.W.M. acknowledges support from the US DOE, Office of Science, Office of Basic Energy Sciences, under award number DE-SC-0012375 for the development of novel ferroic heterostructures. Electron microscopy of superlattice structures was performed at the Molecular Foundry, LBNL, supported by the Office of Science, Office of Basic Energy Sciences, US DOE (DE-AC02-05CH11231). STEM and phase-field analysis and visualization performed by C.T.N. was supported by the US DOE, Office of Science, Basic Energy Sciences, Materials Sciences and Engineering Division. EMPAD-STEM polar mapping at the Cornell Center for Materials Research was funded by the US DOE, grant DE-SC0002334. The Cornell EM Facility is supported by the Cornell Center for Materials Research through the National Science Foundation MRSEC program, award #DMR DMR-1719875.

Author contributions

S.D., Y.L.T. and R.R. designed the experiments. S.D. carried out the synthesis and characterization of the trilayers and superlattice samples via RHEED-assisted pulsed-laser deposition; A.B.M.

synthesized trilayers and superlattice samples by molecular-beam epitaxy with advice from D.G.S. Y.L.T. performed TEM characterization of the samples, along with detailed polarization vector analysis. K.X.N. performed polarization mapping on superlattice films using EMPAD-STEM, supervised by D.A.M. C.T.N. performed STEM and phase-field analysis and visualization. M.A.P.G., F.G.-O., P.G.-F., J.Í. and J.J. completed the second-principles simulations. Z.H. performed phase-field calculations for these samples with strain. R.M., S.D. and V.A.S. carried out the reciprocal space map studies of these samples using synchrotron X-ray diffraction. S.D., M.R.M. and C.K. performed synchrotron X-ray circular-dichroism measurements on these films with P.S. and E.A.'s assistance. R.R., L.W.M., S.D., Y.L.T., Z.H., M.R.M., L.Q.C., P.G.-F., J.Í. and J.J. analyzed the data and co-wrote the manuscript. R.R., L.W.M., L.Q.C. and J.J. supervised the research. All authors contributed to the discussions and manuscript preparation.

References

1. Yadav, A. K. et al. Observation of polar vortices in oxide superlattices. *Nature* **530**, 198–201 (2016); corrigendum **534**, 138 (2016).
2. Damodaran, A. et al. Phase coexistence and electric-field control of toroidal order in oxide superlattices. *Nat. Mater.* **16**, 1003–1009 (2017).
3. Shafer, P. et al. Emergent chirality in polar vortex superlattices. *Proc. Natl Acad. Sci. USA* **115**, 915 (2018).
4. Röbber, U. K., Bogdanov, A. N. & Pfleiderer, C. Spontaneous skyrmion ground states in magnetic metals. *Nature* **442**, 797–801 (2006).
5. Mühlbauer, S. et al. Skyrmion lattice in a chiral magnet. *Science* **323**, 915–919 (2009).
6. Fert, A., Cros, V. & Sampaio, J. Skyrmions on the track. *Nat. Nanotechnol.* **8**, 152–156 (2013)
7. Woo, S. et al. Spin–orbit torque-driven skyrmion dynamics revealed by time-resolved X-ray microscopy. *Nat. Commun.* **8**, 15573 (2017).
8. Tomasello, R. et al. A strategy for the design of skyrmion racetrack memories. *Sci. Rep.* **4**, 6784 (2014).
9. Parkin, S. S. P., Hayashi, M. & Thomas, L. Magnetic domain-wall racetrack memory. *Science* **320**, 190 (2008).
10. Cherifi-Hertel, S. et al. Non-Ising and chiral ferroelectric domain walls revealed by nonlinear optical microscopy. *Nat. Commun.* **8**, 15768 (2017).

11. Lee, D. et al. Mixed Bloch–Néel–Ising character of 180° ferroelectric domain walls. *Phys. Rev. B* **80**, 060102 (2009).
12. Zhang, Q. et al. Nanoscale bubble domains and topological transitions in ultrathin ferroelectric films. *Adv. Mater.* **29**, 1702375 (2017).
13. Lai, B. K. et al. Electric-field-induced domain evolution in ferroelectric ultrathin films. *Phys. Rev. Lett.* **96**, 137602 (2006).
14. Nahas, Y. et al. Discovery of stable skyrmionic states in ferroelectric nanocomposites. *Nat. Commun.* **6**, 8542 (2015).
15. Hong, J., Catalan, G., Fang, D. N., Artacho, E. & Scott, J. F. Topology of the polarization field in ferroelectric nanowires from first principles. *Phys. Rev. B* **81**, 172101 (2010).
16. Gregg, J. M. Exotic domain states in ferroelectrics: searching for vortices and skyrmions. *Ferroelectrics* **433**, 74–87 (2012).
17. Thorner, G. et al. Axial hypertoroidal moment in a ferroelectric nanotorus: a way to switch local polarization. *Phys. Rev. B* **89**, 220103 (2014).
18. Fong, D. D. et al. Ferroelectricity in ultrathin perovskite films. *Science* **304**, 1650–1653 (2004).
19. García-Fernández, P., Wojdeł, J. C., Íñiguez, J. & Junquera, J. Second-principles method for materials simulations including electron and lattice degrees of freedom. *Phys. Rev. B* **93**, 195137 (2016).
20. Mermin, N. D. Topological theory of defects. *Rev. Mod. Phys.* **51**, 591–648 (1979).
21. Tate, M. W. et al. High dynamic range pixel array detector for scanning transmission electron microscopy. *Microsc. Microanal.* **22**, 237–249 (2016).
22. Nelson, C. T. Spontaneous vortex nanodomain arrays at ferroelectric heterointerfaces. *Nano Lett.* **11**, 828–834 (2011).
23. Yu, X. Z. et al. Real-space observation of a two-dimensional skyrmion crystal. *Nature* **465**, 901–904 (2010).
24. Zuo, J. M. & Spence, J. C. H. in *Electron Microdiffraction* Ch. 4 (Plenum Press, New York, 1993).
25. Kirkland, E. J. Computation in electron microscopy. *Acta Crystallogr. A* **72**, 1–27 (2016).
26. Kézsmarki, I. et al. Néel-type skyrmion lattice with confined orientation in the polar magnetic semiconductor GaV4S8. *Nat. Mater.* **14**, 1116–1122 (2015).
27. Lovesey, S. W. & van der Laan, G. Resonant X-ray diffraction from chiral electric-polarization structures. *Phys. Rev. B* **98**, 155410 (2018).

28. Lim, L.-K. & Moessner, R. Pseudospin vortex ring with a nodal line in three dimensions. *Phys. Rev. Lett.* **118**, 016401 (2017).
29. Rayfield, G. W. & Reif, F. Quantized vortex rings in superfluid helium. *Phys. Rev.* **137**, AB4 (1965).
30. Eto, M., Hirono, Y. Nitta, M. and Yasui, S. Vortices and other topological solitons solutions in dense quark matter. *Prog. Theor. Exp. Phys.* **2014**, 012D01 (2014).
31. Ruostekoski, J. J. & Anglin, J. R. Creating vortex rings and three-dimensional skyrmions in Bose–Einstein condensates. *Phys. Rev. Lett.* **86**, 3934–3937 (2001).
32. Lee, W. et al. Synthetic electromagnetic knot in a three-dimensional skyrmion. *Sci. Adv.* **4**, eaao3820 (2018).
33. Rybakov, F. N., Borisov, A. B. & Bogdanov, A. N. Three-dimensional skyrmion states in thin films of cubic helimagnets. *Phys. Rev. B* **87**, 094424 (2013).
34. Yadav, A. K. et al. Spatially resolved steady-state negative capacitance. *Nature* **565**, 468–471 (2019).
35. Chen, L.-Q. Phase-field method of phase transitions/domain structures in ferroelectric thin films: a review. *J. Am. Ceram. Soc.* **91**, 1835–1844 (2008).
36. Hong, Z. et al. Stability of polar vortex lattice in ferroelectric superlattices. *Nano Lett.* **17**, 2246–2252 (2017).
37. Li, Y. L. et al. Effect of substrate constraint on the stability and evolution of ferroelectric domain structures in thin films. *Acta Mater.* **50**, 395–411 (2002).
38. Li, Y. L., Hu, S. Y. & Liu, Z. K. & Chen, L.-Q. Effect of electrical boundary conditions on ferroelectric domain structures in thin films. *Appl. Phys. Lett.* **81**, 427–429 (2002).
39. Haun, M. J. et al. Thermodynamic theory of PbTiO₃. *J. Appl. Phys.* **62**, 3331–3338 (1987).
40. Sheng, G. et al. A modified Landau–Devonshire thermodynamic potential for strontium titanate. *Appl. Phys. Lett.* **96**, 232902 (2010).
41. Chen, L.-Q. & Shen, J. Applications of semi-implicit Fourier-spectral method to phase field equations. *Comput. Phys. Commun.* **108**, 147–158 (1998).
42. Wojdeł, J. C., Hermet, P., Ljungberg, M. P., Ghosez, P. & Íñiguez, J. First-principles model potentials for lattice-dynamical studies: general methodology and example of application to ferroic perovskite oxides. *J. Phys. Condens. Matter* **25**, 305401 (2013).
43. Wojdeł, J. C. & Íñiguez, J. Ferroelectric transitions at ferroelectric domain walls found from first-principles. *Phys. Rev. Lett.* **112**, 247603 (2014).

44. Berg, B. & Lüscher, M. Definition and statistical distributions of a topological number in the lattice $O(3)$ σ -model. *Nucl. Phys. B* **190**, 412–424 (1981).
45. Dürr, H. A. et al. Chiral magnetic domain structures in ultrathin FePd films. *Science* **284**, 2166–2168 (1999).
46. Jiang, W. et al. Skyrmions in magnetic multilayers. *Phys. Rep.* **704**, 1–49 (2017).
47. Bogatyrev, A. B. et al. What makes magnetic skyrmions different from magnetic bubbles? *J. Magn. Magn. Mater.* **465**, 743–746 (2018).

Figures

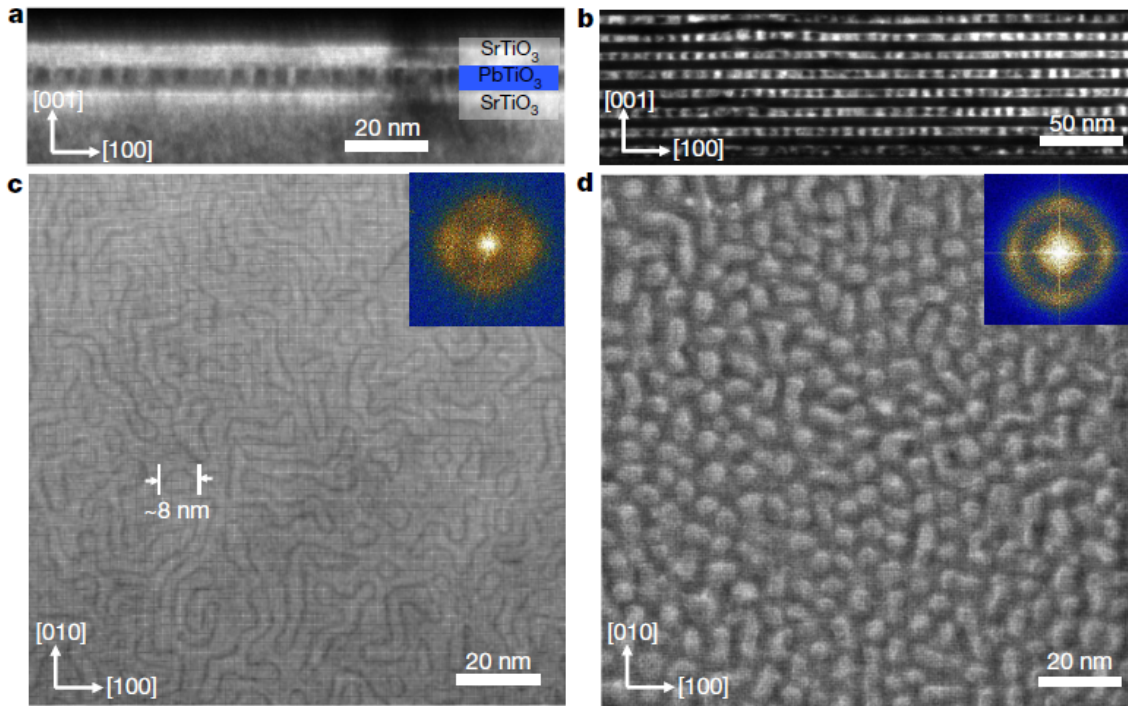


Fig. 1. Observation of ordered polar structure. **a, b,** Cross-sectional dark-field TEM images of a $(\text{SrTiO}_3)_{16}/(\text{PbTiO}_3)_{16}/(\text{SrTiO}_3)_{16}$ trilayer (**a**) and a $[(\text{SrTiO}_3)_{16}/(\text{PbTiO}_3)_{16}]_8$ superlattice (**b**), revealing a regular in-plane modulation of about 8 nm. **c, d,** Planar-view dark-field STEM imaging shows the widespread occurrence of nanometre-size round and elongated features in a $(\text{SrTiO}_3)_4/(\text{PbTiO}_3)_{11}/(\text{SrTiO}_3)_{11}$ trilayer (**c**) and only circular features in a $[(\text{SrTiO}_3)_{16}/(\text{PbTiO}_3)_{16}]_8$ superlattice (**d**) along the $[100]$ and $[010]$ directions. The STEM studies were repeated in a minimum of 10 separate samples and the observations were repeatable. Insets, FFT of the images in c and d show a ring-like distribution with stronger intensities along the cubic directions—the same feature seen in RSM studies.

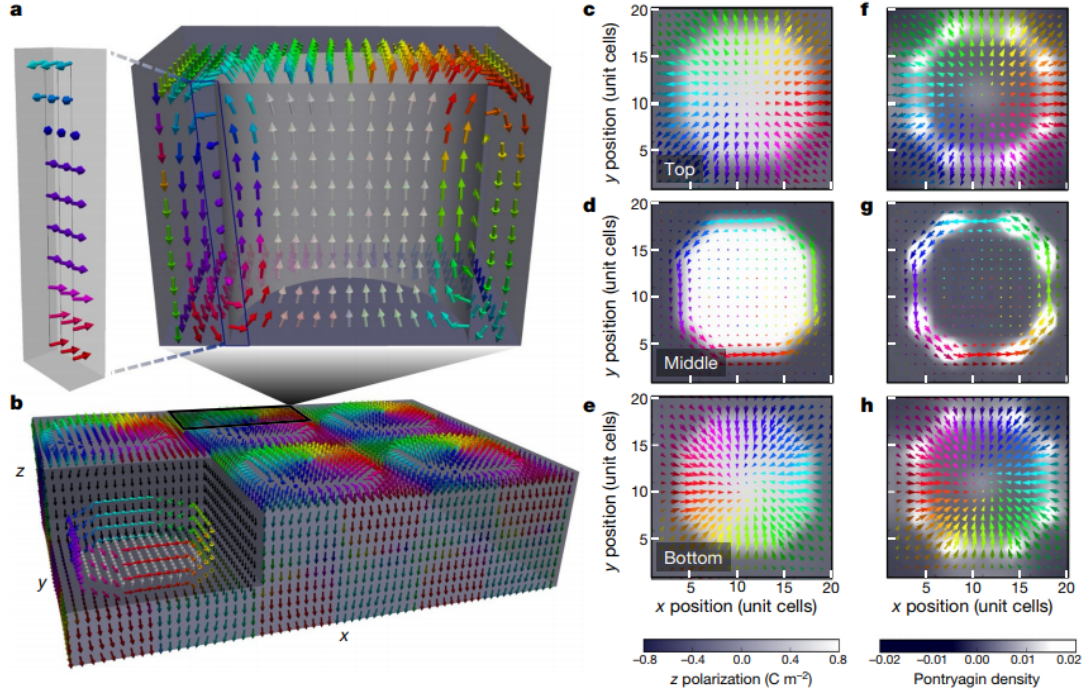


Fig. 2. Second-principles calculations of the skyrmion structure in a $\text{PbTiO}_3\text{-SrTiO}_3$ superlattice. **a**, Right, a cross-section of the polarization texture predicted by second-principles calculations. Bloch walls appear along both the out-of-plane (left) and in-plane directions. **b**, Repetition of the skyrmion structure in the x and y directions, similar to the one observed experimentally (Fig. 1d). The polarization diverges at the top of the structure, rotating smoothly from $+z$ to $-z$ polarization. At the domain wall of the structure, the polarization component rotates in plane, resembling a Bloch skyrmion. **c**, Hedgehog-like skyrmion at the top interface between SrTiO_3 and PbTiO_3 . **d**, Bloch skyrmion at the central plane in PbTiO_3 . **e**, Hedgehog-like skyrmion at the bottom interface. The up and down domains are represented by white and grey regions, respectively. **f-h**, The corresponding Pontryagin densities. The arrows represent the normalized electric dipole moments in the x - y plane.

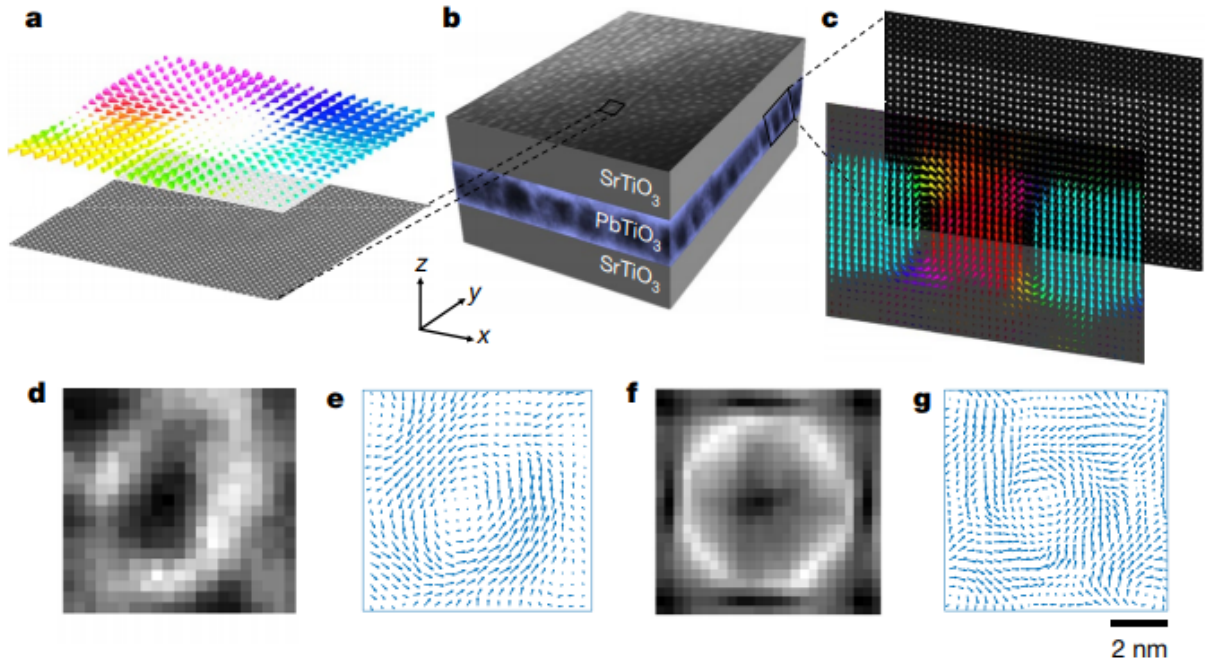


Fig. 3. Observation of polar-skyrmion structure. **a, b**, Reversed Ti-displacement vector map (top) based on the atomically resolved plane-view HAADF-STEM image (bottom) of a single skyrmion bubble (marked by a white circle in Extended Data Fig. 6a), showing the hedgehog-like skyrmion structure. The sketch of the superlattice in **b** is overlaid with the planar-view dark-field TEM image and gives a top view of the superlattice. **c**, Ti-displacement vector map (front) based on the atomically resolved cross-sectional HAADF-STEM image (back), showing a cylindrical domain with anti-parallel (up-down) polarization. The sketch in **b** is overlaid with the cross-sectional dark-field TEM image and shows the cross-sectional view of the superlattice. **d, e**, The 4D-STEM image of a $[(\text{PbTiO}_3)_{16}/(\text{SrTiO}_3)_{16}]_8$ superlattice gives the ADF image (**d**) and maps of polar order using the probability current flow (**e**), which were reconstructed from the same 4D dataset. **f, g**, Multislice simulations of the beam propagation through the model structure from Fig. 2 show the ADF image (**f**) and the probability current flow (**g**), which were analyzed using the same process as the experimental data. The signals are not simple projections, but weighted by electron beam channelling towards the middle of the skyrmion bubble, where the polarization exhibits a Bloch like character.

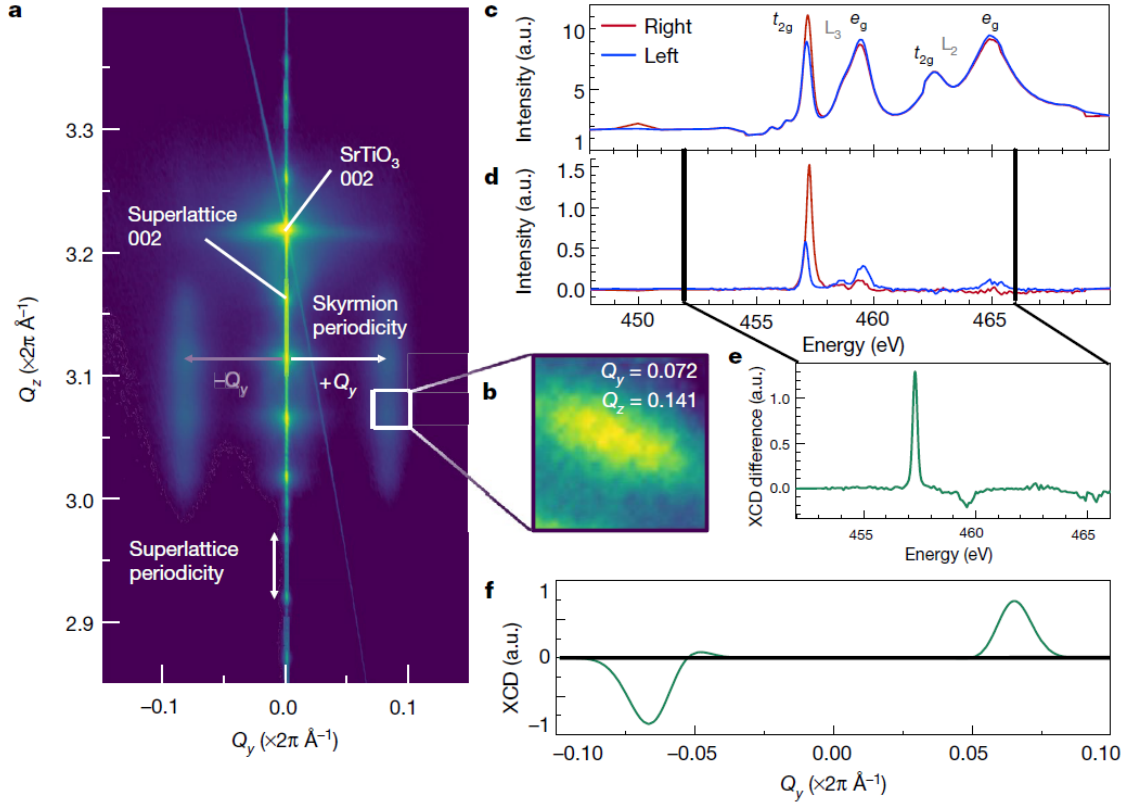
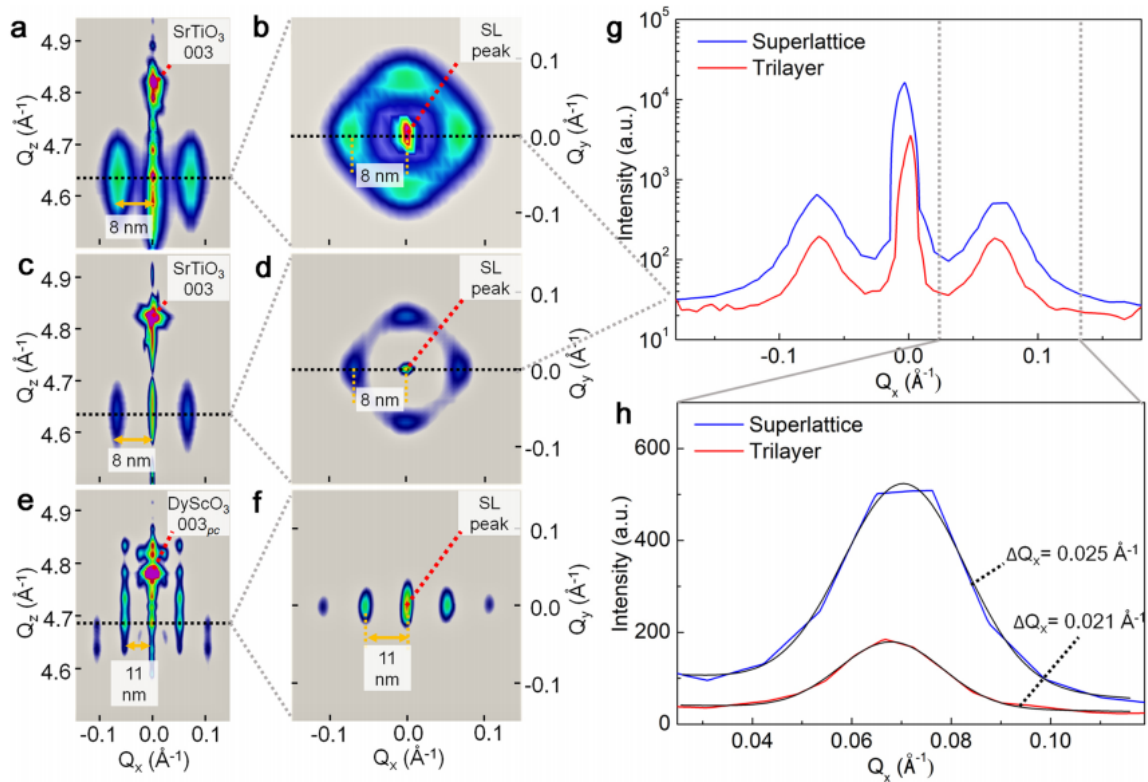


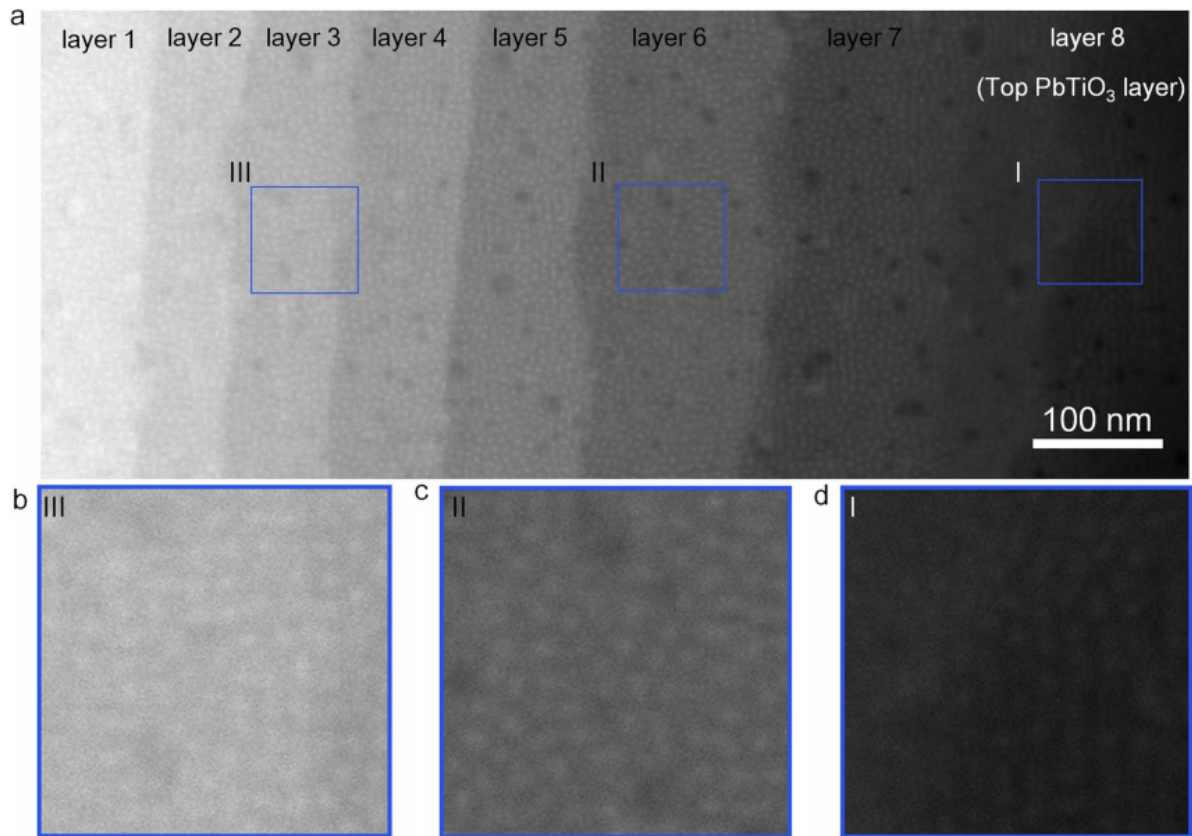
Fig. 4. RSXD circular dichroism. **a**, Hard-X-ray reciprocal space mapping about the SrTiO₃ (002) peak for a [(PbTiO₃)₁₆/(SrTiO₃)₁₆]₈ superlattice shows superlattice peaks along the Q_z direction, corresponding to an out-of-plane periodicity of about 12 nm, and satellite peaks along the Q_y direction, corresponding to an in-plane periodicity of about 8 nm. **b**, An image from the charge-coupled device (CCD) used to collect RSXD data, with the resonant diffraction peak clearly visible. The satellite peaks accessible by RSXD are near $(Q_x, Q_y, Q_z) = (0, 0, \ll 2\pi/c)$, and the satellite peak shown is at around $Q_y = 0.072 \text{ \AA}^{-1}$ and $Q_z = 0.141 \text{ \AA}^{-1}$, corresponding to the periodic helical polarization texture that forms within the Bloch skyrmions of the central PbTiO₃ layers. **c,d**, Spectra from a satellite peak for right- (red) and left-circularly (blue) polarized light (**c**) and the same spectra with the background fluorescence subtracted (**d**). The peaks corresponding to the L_3 and L_2 transitions to the t_{2g} and e_g states are labelled. **e**, The XCD difference spectrum (right-circular minus left-circular X-ray absorption spectrum) shows a clear circular dichroism peak at the titanium L_3 t_{2g} edge. **f**, XCD measured at a constant energy (457.4 eV) near resonance as the lateral-scattering vector Q_y is varied. The dichroism is always positive for $+Q_y$.

and negative for $-Q_y$. The reversal of XCD as the Q -vector is inverted is a tell-tale signature of chirality. a.u., arbitrary units.

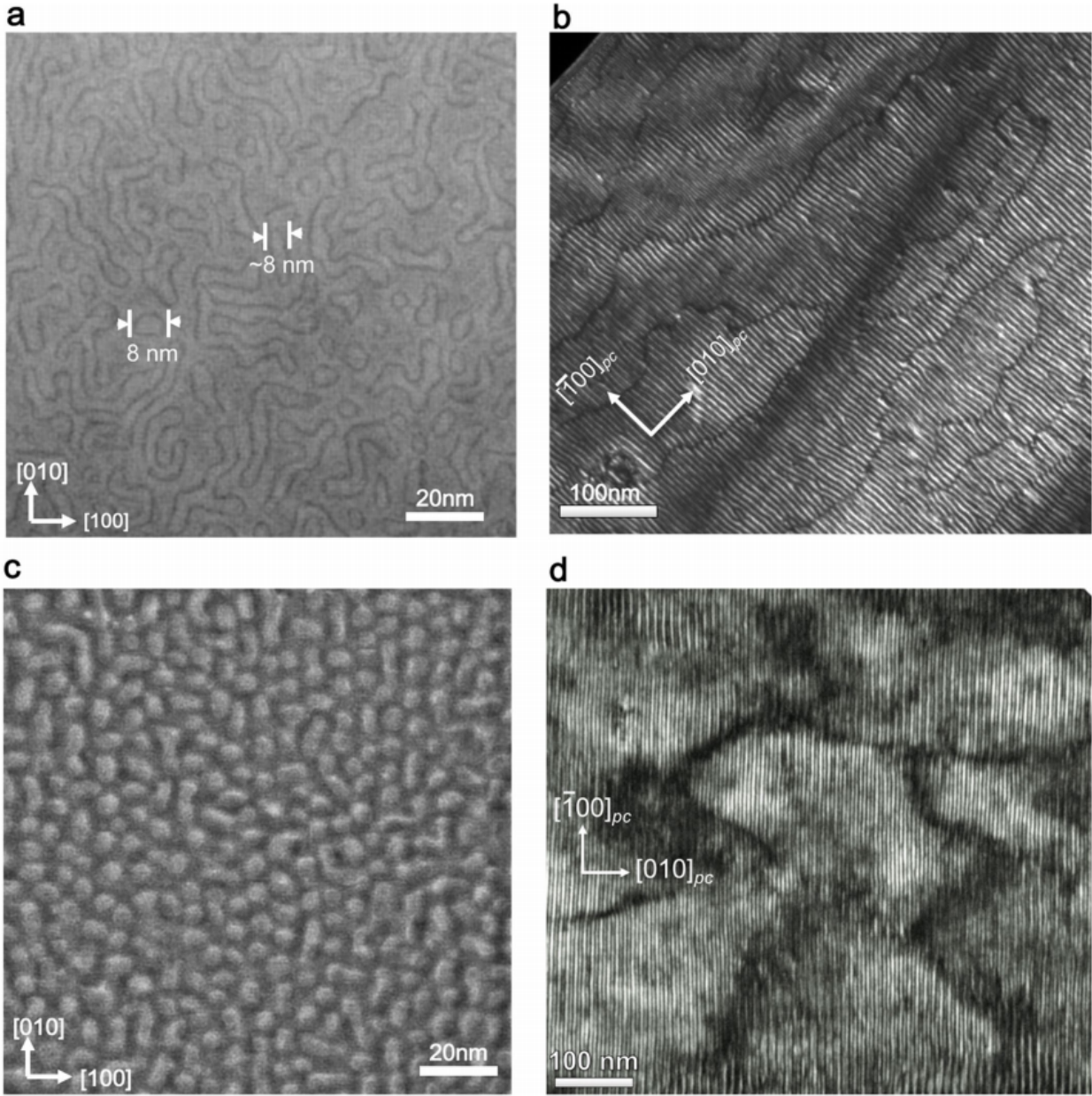


Extended Data Fig. 1. Three-dimensional reciprocal space mapping. **a-f**, RSM of the specular peak for the $[(\text{PbTiO}_3)_{16}/(\text{SrTiO}_3)_{16}]_8$ superlattice (SL; **a** and **b**) and the $(\text{SrTiO}_3)_{16}/(\text{PbTiO}_3)_{16}/(\text{SrTiO}_3)_{16}$ trilayer (**c** and **d**) on a SrTiO_3 (001) substrate and for the $[(\text{PbTiO}_3)_{16}/(\text{SrTiO}_3)_{16}]_8$ superlattice on a DyScO_3 (110) substrate (**e-f**). Near the (003) diffraction condition in **a** and **c**, satellite peaks, assigned to polar ordering in PbTiO_3 , are detected along the in-plane directions, and their lateral characteristic size is about 8 nm and proportional to $1/Q_x$ at the satellite position. **b**, **d**, In-plane RSM cuts (taken at the dashed black line in **a** and **c**) show a preferential fourfold intensity distribution along the cubic directions of the substrate, which overlaps with a diffuse scattering ring – a pattern that is more intense in the superlattice sample compared to the trilayer sample. **g**, In-plane line scan data from the dashed lines in **b** and **d** are plotted together for the superlattice and trilayer samples. **h**, Gaussian line profile analyses of the satellite peaks (fitting functions are plotted as black lines) provide peak positions and peak widths at the half intensity maximum (ΔQ_x), which are found to be similar in the superlattice and trilayer samples grown on the SrTiO_3 (001) substrate. The similar sizes of the diffuse-scattering rings (about 8 nm) and the in plane-widths, as well as the same vertical position (Q_z) of the diffuse-scattering patterns in the superlattice and trilayer samples, show that the polar-ordering states have

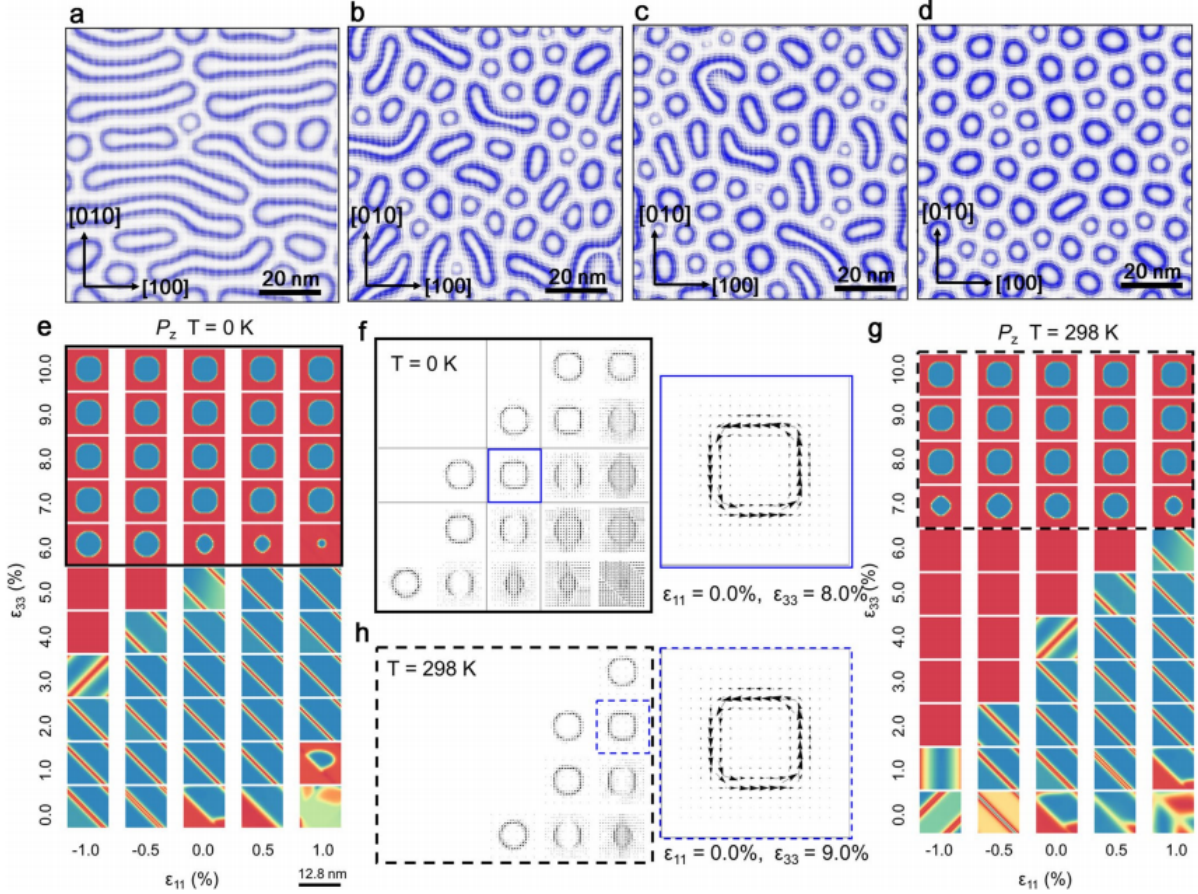
common origin in these samples. By contrast, the reciprocal space maps of the polar-vortex structure in the $[(\text{PbTiO}_3)_{16}/(\text{SrTiO}_3)_{16}]_8$ superlattice on DyScO_3 (110) shown in **e** around the $(003)_{\text{pc}}$ (pc, pseudo-cubic) peak exhibit highly anisotropic in-plane peak satellites, including higher-order peak satellites, which correspond to vortex array ordering with periodicity of about 11 nm, as shown in more detail in the in-plane cut from **f**, which is taken at the Q_z value indicated by the dashed line in **e**.



Extended Data Fig. 2. Under-focus STEM imaging of polar-skyrmion bubbles across the entire $[(\text{PbTiO}_3)_{16}/(\text{SrTiO}_3)_{16}]_8$ superlattice. a, The full image. **b-d**, Magnifications of areas I, II and III labelled in **a**, showing that the skyrmion bubbles formed in all of the PbTiO₃ layers.

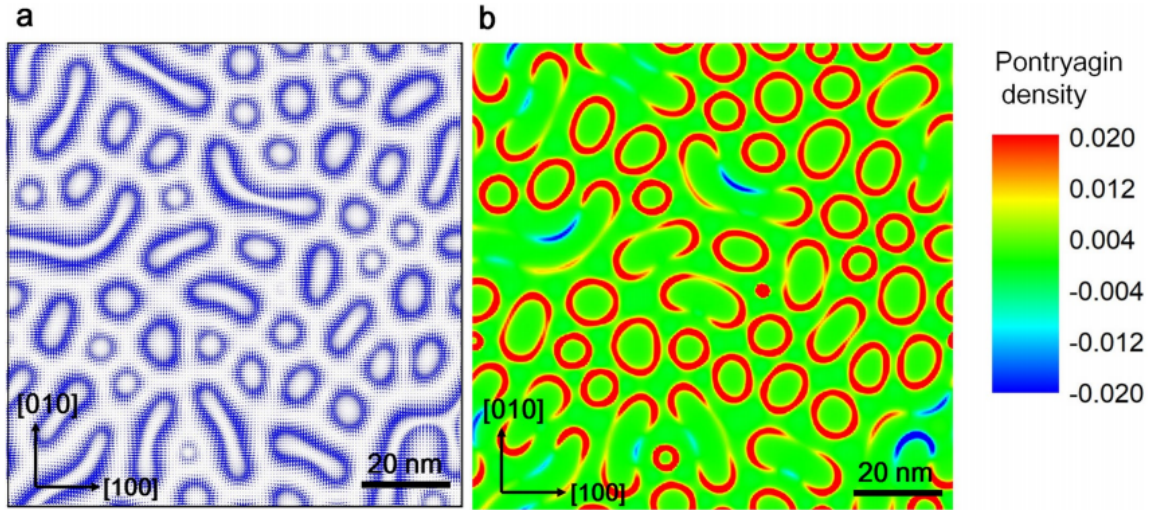


Extended Data Fig. 3. Planar-view dark-field STEM imaging. **a, c**, Planar-view dark-field STEM images of $(\text{SrTiO}_3)_{16}/(\text{PbTiO}_3)_{16}/(\text{SrTiO}_3)_{16}$ trilayers (**a**) and the $[(\text{PbTiO}_3)_{16}/(\text{SrTiO}_3)_{16}]_8$ superlattice (**c**) on SrTiO_3 (001), showing the widespread occurrence of nanometre-size skyrmion bubbles and elongated-skyrmion-like features along the [100] and [010] directions. **b, d**, Planar-view dark-field STEM images of $(\text{SrTiO}_3)_{16}/(\text{PbTiO}_3)_{16}/(\text{SrTiO}_3)_{16}$ trilayers (**b**) and the $[(\text{PbTiO}_3)_{16}/(\text{SrTiO}_3)_{16}]_8$ superlattice (**d**) on DyScO_3 (110), showing the long-range in-plane ordering associated with the clockwise–counterclockwise vortex stripe along $[100]_{pc}$ and confirming the widespread occurrence of these vortex stripes in the trilayers and superlattice films on DyScO_3 (110) substrates.

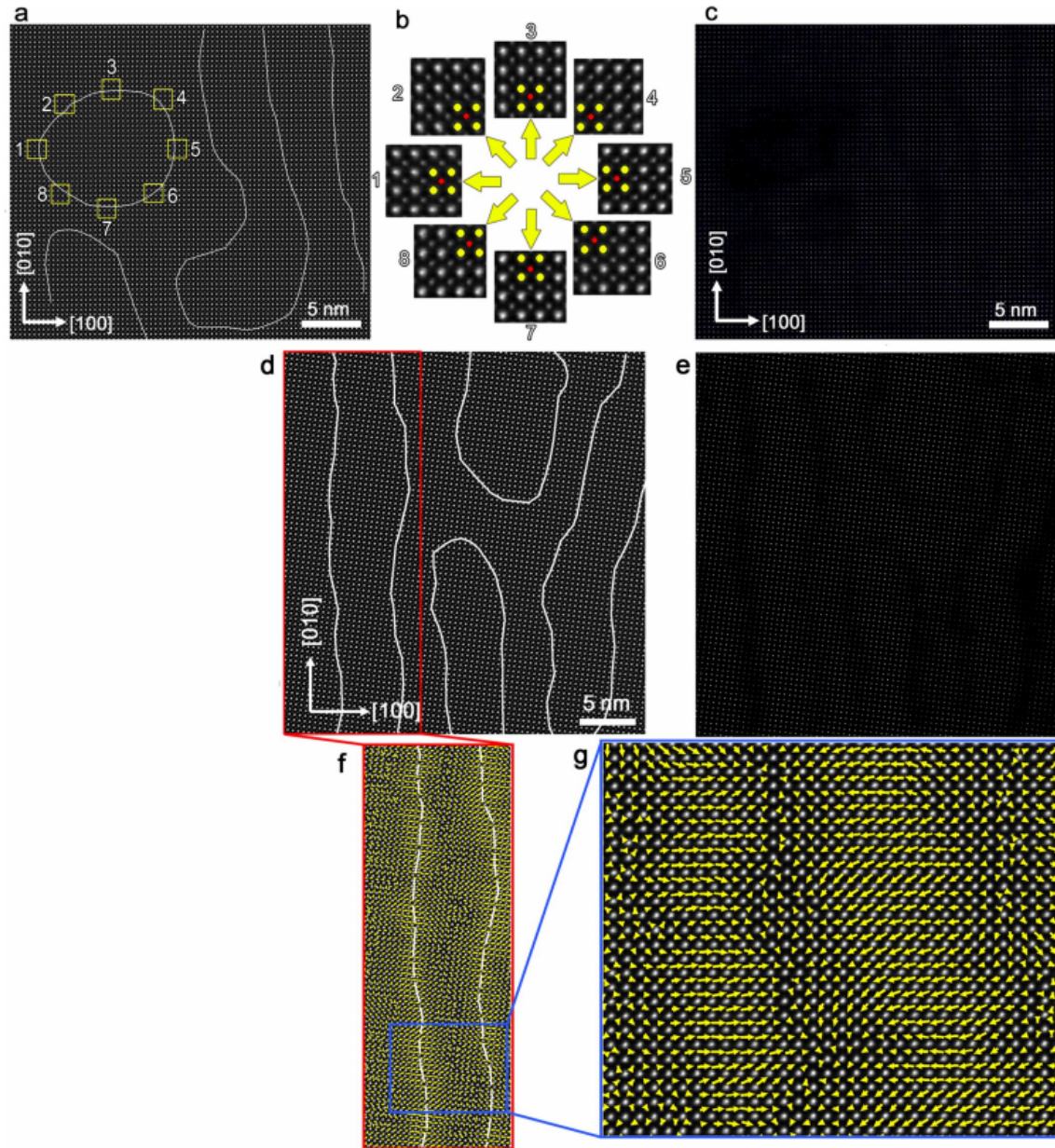


Extended Data Fig. 4. Phase-field simulation of topological polar structure of $(\text{SrTiO}_3)_{16}/(\text{PbTiO}_3)_{16}/(\text{SrTiO}_3)_{16}$ trilayer and $[(\text{PbTiO}_3)_{16}/(\text{SrTiO}_3)_{16}]_m$ ($m = 3-8$) superlattices with different total film thickness. a-d, Planar view of the $(\text{STO})_{16}/(\text{PTO})_{16}/(\text{STO})_{16}$ trilayer (a), showing that skyrmion bubbles (diameter of about 8 nm) coexist with elongated skyrmions (length, about 40 nm; diameter, about 8 nm) – long closed vortex-line-like structures. By increasing the number of PTO layers to the $[(\text{PbTiO}_3)_{16}/(\text{SrTiO}_3)_{16}]_3$ (b) and $[(\text{PbTiO}_3)_{16}/(\text{SrTiO}_3)_{16}]_5$ (c) superlattices, it is observed that the elongated skyrmions become smaller and the skyrmion-bubble density increases. The density of skyrmion bubbles continues to increase until it reaches almost 100% for the $[(\text{PbTiO}_3)_{16}/(\text{SrTiO}_3)_{16}]_8$ superlattice (d). Interestingly, the size of the skyrmion bubbles in all these systems barely changes. This is a demonstration of a thickness-driven Rayleigh-Plateau instability, where the longer vortex-line like structure decomposes into small skyrmion bubbles. These features closely match the experimental observations. The blue markers represent in-plane polarization (P_{ip}), whereas the white regions have out-of-plane polarization (P_{op}). Here, the interior of the skyrmion has P_{op} out of the page,

which rotates in-plane (P_{ip}) to the edge of the skyrmion. **e-g**, Phase-field simulation of the central plane in a PbTiO_3 layer. **e**, The out-of-plane polarization (P_z) of the skyrmion bubble in the PbTiO_3 layer at 0 K under various in-plane (ϵ_{11}) and out-of-plane (ϵ_{33}) strain states. **f**, The in-plane polarization distribution for different strain states in the selected region (black solid rectangle) of **e** reveals the finite Bloch component. **g**, The out-of-plane polarization (P_z) of the skyrmion bubble in the PbTiO_3 layer at 298 K under various strain states. **h**, The in-plane polarization distribution of different strain states in the selected region (black dashed rectangle) of **g** reveals the finite Bloch component.

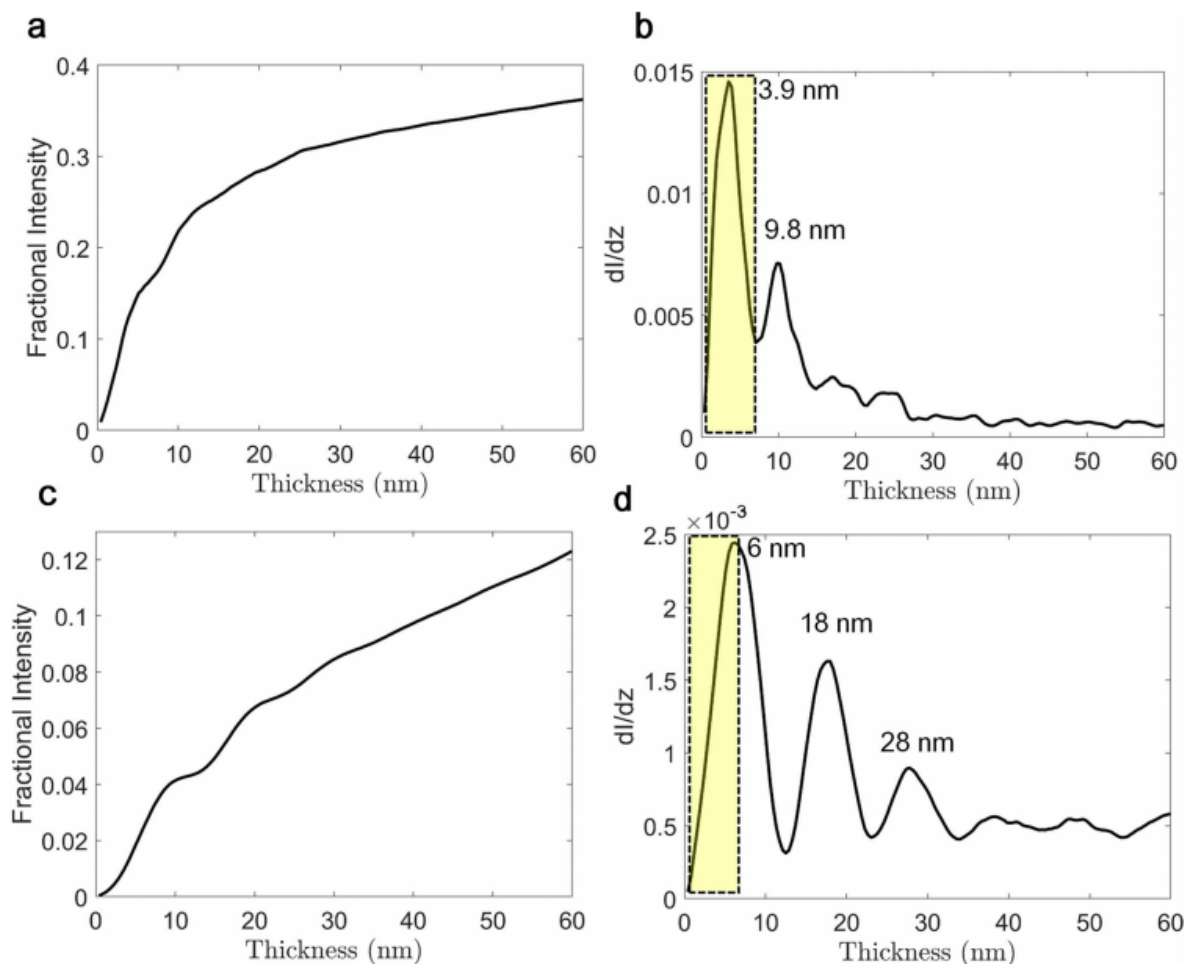


Extended Data Fig. 5. Pontryagin density distribution from phase-field simulations of skyrmion bubbles and elongated skyrmions for the $[(\text{PbTiO}_3)_{16}/(\text{SrTiO}_3)_{16}]_3$ superlattice. a, Planar view of the $[(\text{PbTiO}_3)_{16}/(\text{SrTiO}_3)_{16}]_3$ superlattice, showing coexistence of skyrmion bubbles with elongated-skyrmion features. **b,** The corresponding Pontryagin density calculation. Skyrmion bubbles have a circular shape, indicating a radial distribution of the polar texture, whereas the elongated-skyrmion features have larger density in the two ends and both positive and negative values in the middle. The surface integration gives a topological charge value of +1 for both the skyrmion bubbles and the elongated skyrmions, so the elongated-skyrmion features and the skyrmion bubbles are topologically equivalent structures.

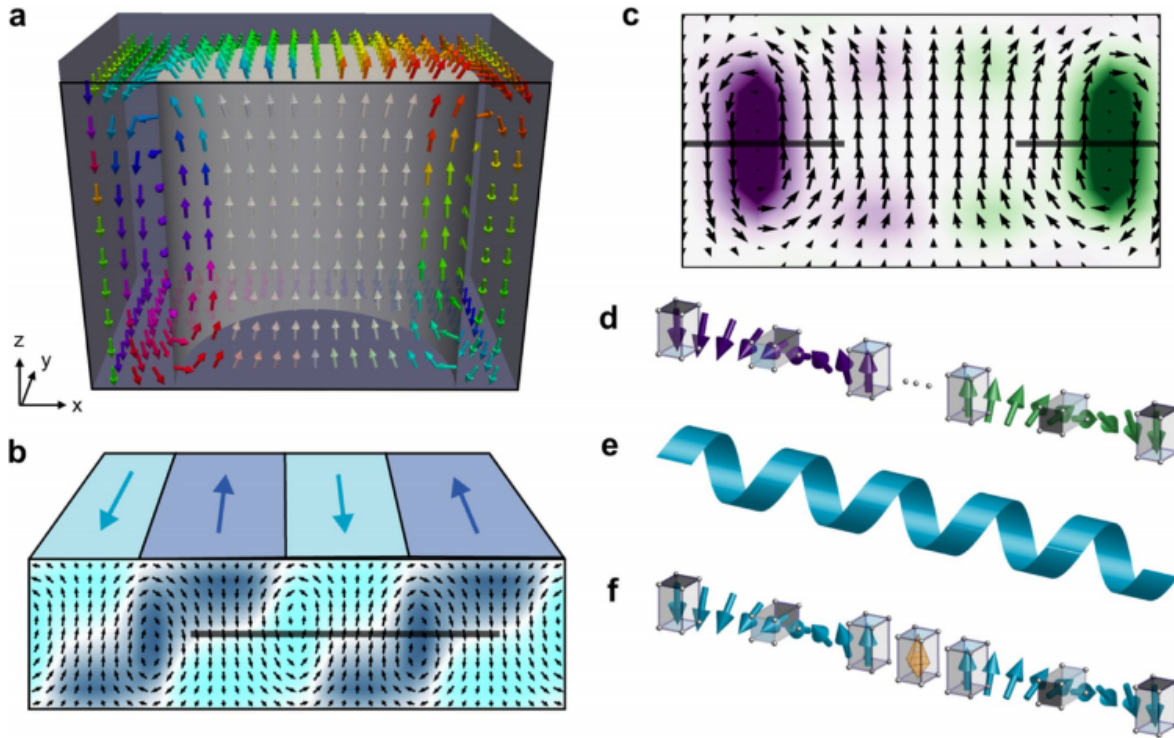


Extended Data Fig. 6. High-resolution HAADF-STEM imaging. **a**, Atomically resolved plane-view HAADF-STEM image of the $(\text{SrTiO}_3)_{16}/(\text{PbTiO}_3)_{16}/(\text{SrTiO}_3)_{16}$ trilayer. **b**, Enlarged PbTiO_3 unit cells around the circular domain, showing the Ti shifts directly, as marked by yellow boxes in **a**. We note the diverging Ti-displacement vector configuration marked with a box. The domain walls are roughly sketched in **a** (marked by white lines) according to the Ti-displacement map. **c**, False-color representations of **a**. The enhanced contrast facilitates the visualization of the skyrmion bubble and domain walls because of the remnant diffraction contrast, where the ferroelectric domain walls can be seen by the naked eye. **d-g**, Ti-cation-displacement vector maps based on the

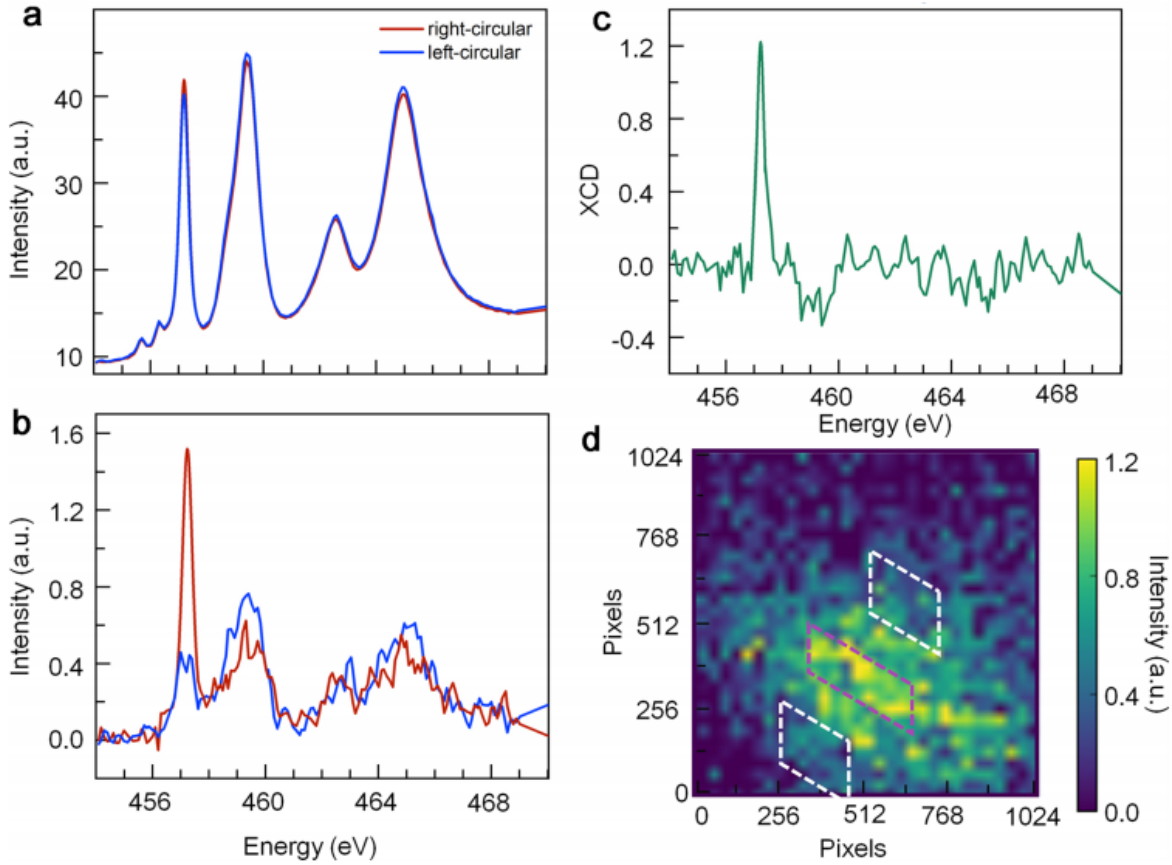
plane-view HAADF-STEM images showing the domain walls. **d**, Atomically resolved HAADF-STEM image. White lines denote domain walls. **e**, A false-color representation of **d**. The enhanced contrast facilitates the visualization of the domain walls because of the remnant diffraction contrast, where the ferroelectric domain walls can be seen by the naked eye. **f**, Superposition of Ti-shift vectors with the HAADF image of the area in **d** marked with a red box. Dashed lines denote the domain walls. **g**, An enlarged area of the Ti-shift mapping in **f** (marked by a blue box), showing the domain walls. Yellow arrows denote Ti-displacement directions. The displacement of Ti cations at the ferroelectric domain walls can be seen clearly.



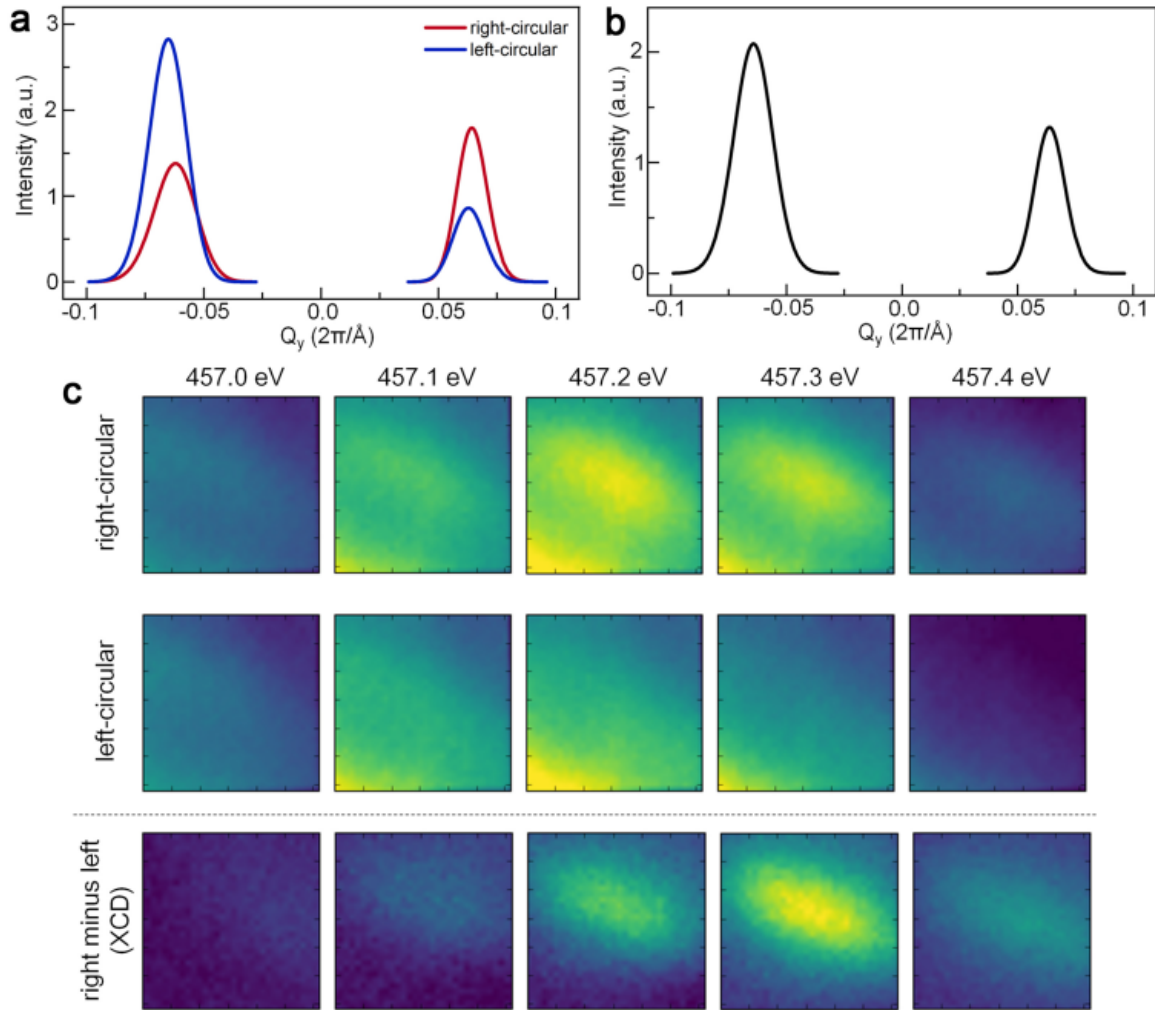
Extended Data Fig. 7. Electron beam channelling along a column of Sr atoms in SrTiO₃. **a**, High-angle ADF signal (50-200 mrad) $I(z)$ for a 300-keV electron beam centred on the Sr site as a function of depth, z , into the crystal, with a 17.2-mrad convergence angle, similar to that used in the HAADF experiments to resolve individual atoms. **b**, The derivative of the HAADF signal, showing that the peak signal is generated at 3.9 nm or about 10 unit cells into the SrTiO₃. The signal is close to the minimum at 16 unit cells, indicating a strong dechannelling at the point where PbTiO₃ would begin in a multilayer structure. **c**, The HAADF signal for a 1.7-mrad convergence angle, similar to that used in the EMPAD experiments to separate diffraction disks. **d**, From the derivative dI/dz , the signal is still channeling efficiently at the point where the PbTiO₃ would begin in a multilayer structure. Thus, the EMPAD setup couples more efficiently to the PbTiO₃. The yellow box shows the thickness of 16 unit cells of SrTiO₃, the thickness of the repeated cell in the 16×16 multilayer.



Extended Data Fig. 8. Chiral textures of the polarization. **a, b**, Three-dimensional cross-sectional view of a polar-skyrmion bubble (**a**) and chiral polar-vortex structures₃ (**b**). **c**, The cross-section in the middle of the polar-skyrmion bubble (from the black box in **a**), where the green and purple coloring represents the in-plane component along the positive and negative y direction, respectively. **d-f**, An expanded view of the polarization at the center of the skyrmion bubble (marked by black lines in **c**), showing how the polarization rotates in a helical (Bloch-like) fashion along the in-plane direction (**d**). This is virtually identical to the helical rotation of the polarization (**e, f**) that is observed at the center (marked by the black line in **b**) of chiral polar-vortex structures.



Extended Data Fig. 9. RSXD for a trilayer sample. **a**, Spectra of right- (red) and left- (blue) circularly polarized light at the satellite diffraction peak. **b**, The same spectra for the trilayer sample after background fluorescence is subtracted. **c**, The difference of the spectra (XCD) shown in **b**, which shows strong dichroism at the $L_3 t_{2g}$ edge. **d**, The intensity difference of two CCD images measured at the t_{2g} resonance with opposite circular polarizations. The result clearly shows the circular dichroism at the satellite peak. This localization of dichroism at the diffraction peak indicates that the dichroism comes from periodic chiral structures in the sample. Data for the peak and background were measured at the regions marked in magenta and white, respectively.



Extended Data Fig. 10. RSXD polarization-averaged intensity for a $[(\text{PbTiO}_3)_{16}/(\text{SrTiO}_3)_{16}]_8$ superlattice. **a**, Scattering of right- (red) and left- (blue) circularly polarized X-rays from polar skyrmions. The diffraction data were collected along the in-plane (Q_y) direction at the third-order superlattice reflection ($Q_z = 0.16 \text{ \AA}^{-1}$). These peaks are the (013) and (013) peaks of the skyrmion lattice. **b**, The polarization-averaged intensity from RSXD studies reveals an asymmetry in the (013) and (013) diffraction peaks. The asymmetry of the scattered intensity indicates that the polar structures are chiral and consistent with an in plane Bloch component. **c**, RSXD images for a superlattice. Images from the two-dimensional CCD used to collect diffraction data for right- (top row) and left- (middle row) circularly polarized light. A strong enhancement in diffraction intensity is observed around 457.2 eV, at the $L_3 t_{2g}$ resonance, particularly for right-circularly polarized light. The XCD can be visualized by the difference of the images of right- and left circularly polarized light (bottom row).